Visual Abstract

Study of the slant fracture in solid and hollow cylinders: Experimental analysis and numerical prediction

N. Ben Chabane, N. Aguechari, M. Ould Ouali*
Laboratoire LEC2M, Mouloud MAMMERI University, BP17RP, 15000 Tizi Ouzou, Al.
benchabane-nassima@hotmail.fr, naguechari@cds.asal.dz
Mohand.ouldouali@ummto.dz, http://orcid.org/0000-0001-7958-4974

ABSTRACT. This paper is devoted to the numerical and experimental study of ductile fracture in bulk metal forming of the 2017A-T4 aluminum alloy. From an experimental standpoint, the ductile fracture of the2017A-T4aluminum alloy is investigated under compressive load. Two cross-sections of solid and hollow specimens are considered. The mechanical behavior and the microstructure of the 2017A-T4 aluminum alloy were characterized. It is found that the well-known barrel shape is obtained when a compressive load is applied. Analyses of fracture topographies show a ductile fracture with dimples under tension and coexistence of ductile fracture with dimples and slant under compression. The classical physically-based Gurson-Tvergaard-Needleman (GTN) model and its extension to incorporateshear mechanisms to predict failure at low-stress triaxiality are considered. These two models have been extended to take into account the thermal heating effect induced by the mechanical dissipation within the material during the metal forming process. The two models have been implemented into the finite element code Abaqus/Explicit using a Vectorized User MATerial (VUMAT) subroutine. Numerical simulations of the forging process made for hollow and solid cylindrical specimens show good agreement with experimental results. In contrast with the GTN model, the modified GTN model incorporating shear mechanisms can capture the final material failure.

KEYWORDS. Physically-based model, Ductile fracture, Thermomechanical coupling, Slant fracture, Shear mechanisms, Numerical implementation.

OPEN ACCESS

Citation: Ben Chabane, N., Aguechari, N., Ould Ouali, M., Study of the slant fracture in solid and hollow cylinders: Experimental analysis and numerical prediction, Frattura ed Integrità Strutturale, 63 (2023) 169-189.

Received: 31.07.2022
Accepted: 06.11.2022
Online first: 22.11.2022
Published: 01.01.2023

INTRODUCTION

The use of aluminum alloys is widespread in mechanical industries like construction and transport. This is due to the lightweight high-strength properties of these materials. Aluminum alloy forgings are usually produced in a more highly refined final forging shape than forged carbon and/or steel alloys. The pressure requirements for forging vary widely for a given aluminum alloy. It depends namely on the chemical composition of the alloy, the forming

process being employed and the strain rate, the lubrication conditions, and the temperatures adopted. Aluminum alloys of the 2xxx series are widely used in modern industries such as aerospace and automotive applications. This is due to their good resistance properties associated with their lightness and good castability, formability, and weldability, see for instance [1-4].

In the last decades, many efforts have been made to understand the plasticity and damage behavior of metallic materials as well as their effect on stress flow. This understanding is essential for several processes like metal forming and welding, high-speed machining, impact, energy absorption, penetration, and shear localization, see for instance [5-8]. For damage prediction and in comparison with the modeling adopting the concept of continuum damage mechanics (CDM), the damage approach to the growth of microvoids has met considerable success these last years. Indeed, isotropic and anisotropic models developed in the framework of this last approach, which consists of modeling the three successive physical mechanisms: the voids nucleation, their growth, and coalescence of neighboring voids are greatly in use today. Germination and growth of voids have been both experimentally studied and theoretically analyzed using micromechanical methods. In 1975, Gurson proposed a pioneer physically-based model based on limit analysis of spherical voids embedded in a perfectly plastic matrix [9]. This damage-by-cavitation model shows some limitations regarding the over-prediction of the microvoids evolution at final material rupture. As a result, several extensions have been made either based on the improvement of the results at low porosities or the modification of its yield function in order to describe the effects of rate loading, material instabilities, and final rupture by voids coalescence [10-14]. Numerous isotropic and anisotropic damage models have been proposed by many authors to improve numerical predictions or to consider other physical mechanisms [14-20]. It is obvious that a constant void volume fraction is not sufficient in describing the fracture. Pardoen and Hutchinson [21] concluded that the void volume fraction is not constant at fracture for different loading conditions. The damage accumulation in the loading direction represents a three-dimensional problem in which pressure, the Lode angle, and equivalent stress level affect the damage rate. Nahshon and Hutchinson [22] modified the porosity evolution law to account for material damage at low or vanishing triaxiality. Wierzbicki and Xue [23] modified Wilkins' model [24], incorporating the effect of the Lode angle on the ductile fracture.

Descriptions of material mechanical behavior during the forming process are of great industrial interest, especially in terms of manufacturing process optimization. Investigation of damage mechanisms in mechanical parts throughout such operations should prevent the internal or surface cracks initiation as well as their propagation before the overall failure of a structure. In this paper, experimental and numerical studies are presented, focusing on ductile fracture in forged bulk metal made from 2017A-T4. The study of the workpiece behavior in processing conditions needs to characterize the material microstructure, the flow stress evolution, and the rupture mechanisms. In the damage-plasticity concept, the GTN model has been extended to incorporate the effect of the lode angle in order to include the thermal heating due to plastic dissipation. Thermal softening is generally observed in the bulk metal forming process and is considered as favouring the formation of shear bands [25-27]. This model is implemented into the finite element code Abaqus using a typical sequentially coupled thermal-stress algorithm. Predictions of the damage, and therefore the final failure of structures under compressive load represent one of the major goals of this paper. Several numerical simulations are conducted describing the bulk aluminum alloy behavior during the forming process

EXPERIMENTAL ANALYSIS

The damage mechanism is a complicated process. It is well known that quantitative experimental analysis is not a direct and simple task for determining the damage parameters. An experimental program is proposed to show the adopted methodology. The selected material here is the aluminum alloy 2017A-T4 used in aeronautics and automobile industries. The experimental program includes a set of solid and hollow cylinders tested under compressive loads. The determination of material fracture parameters is realized by a methodology based on a coupling between the experimental program and numerical prediction. Moreover, the use of the scanning electron microscopy (SEM) technique is essential for studying fracture behavior.

Chemical composition

The chemical composition of the employed material is summarized in Tab. 1. A and R are referred to Axial and Radial directions for the cylinder, respectively. The observed metallurgical phases present in the aluminum alloy are also shown with respect to axial (A) and radial (R) directions. In Fig. 1, it is recognized that the formation of slip bands in the A direction is due to the extrusion effects with which the bar is produced. With the microstructure of the alloy, a solid solution of copper in aluminum (α-Al) in white and grey consists mainly of aluminum and a phase of θ-Al_2Cu (in black) is

also observed (Fig. 1). The XRD specter analysis given in Fig. 2 shows the metallurgical phases presented by this alloy. The inter-metallic particles of Al_2Cu and Al_2CuMg phases are also recorded.

Elements	Cu	Mg	Mn	Si	Fe	Zn	Al
wt %	4.33	0.93	0.58	0.99	0.70	0.21	92.24

Table 1: Chemical composition of the 2017A-T4.

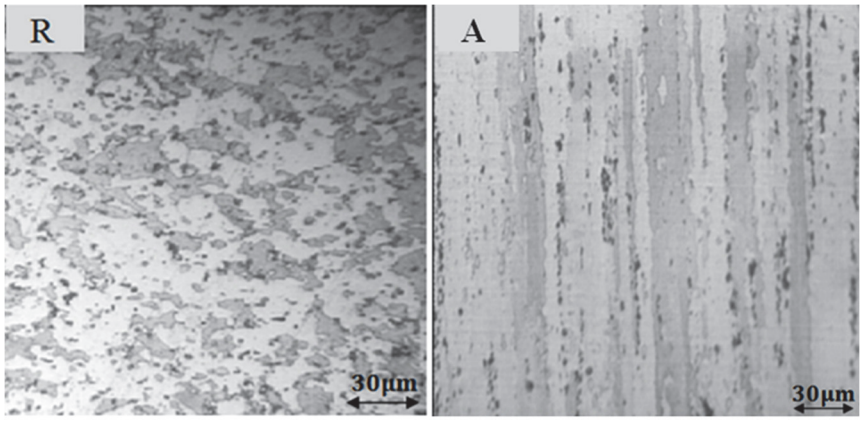

Figure 1: Microstructures of the 2017A-T4aluminum alloy observed after chemical preparation in the radial (R) and axial (A) directions.

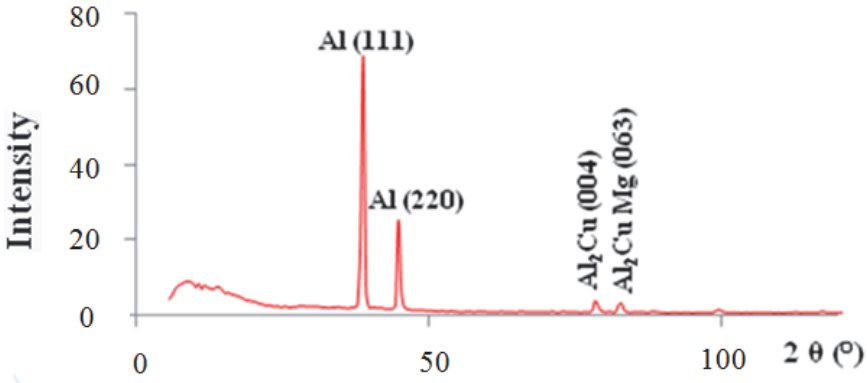

Figure 2: X-Ray Diffractogram (XRD) of 2017A-T4.

Examination of the initial microstructure

The microstructure of the alloy is studied and analyzed through two samples before and after the chemical preparation using an optical microscope as shown in Fig. 3. In this alloy, a wide range of particles acting as sites for void nucleation is observed. Forming during casting, these particles can be classified into two types regarding their size. The first type concerns large inclusions with a range of diameters from ~1 to 10 µm; whereas for the second one (small inclusions-dispersoids), their diameters vary from ~0 to 1µm. Note that the characterization of the particles' density is required to determine the initial porosity denoted f_0 based on these particles. f_0 is considered a damage parameter in the micromechanical approach for fracture [9-11]. It can be defined starting from the volume fraction of particles f_p using the following expression [28-30]:

$$f_0 = W_0 f_p \tag{1}$$

where W_o is the parameter of the mean particle shape. The surface fraction of inclusions f_p is measured by image processing software "Image J".

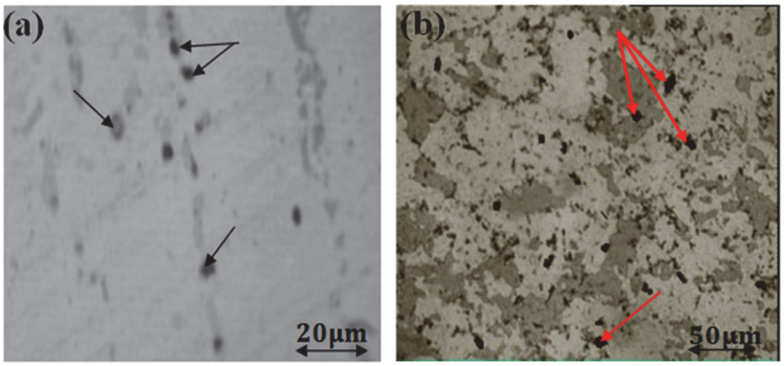

Figure 3: Second-phase inclusion distribution observed by optical microscopy in 2017A-T4: (a) before and (b) after chemical preparation.

Mechanical tests

One of the mechanical tests is microhardness. It is performed by Vickers indentation with a 300g load. The recorded values are reported in Fig. 4. An examination of this figure points out that the values in axial and radial directions have almost the same average and their values are given in Tab. 2. Several mechanical properties of the alloy are determined by means of tensile tests. They are carried out using standardized cylindrical specimens (NFA 401) (Fig. 5). All the tests are loaded under a crosshead speed of 5mm/min at room temperature using a universal servo-hydraulic testing machine of WOLPERT AMSLER TZZ220 having a maximum loading capacity of ± 200 kN with Zwick/RoellZmart.Pro electronic command. The reliability and accuracy of the experimental results should be considered. Therefore, the tests are repeated three times at least with the same loading speed. If the differences between the three responses exceed 3%, then another test should is conducted under the same experimental conditions. The typical stress-strain curve for this alloy is shown in Fig. 6. Tab.3sums up the mechanical characteristics of the alloy.

Forging tests are also realized to further identify the material and structure behavior. All the cylindrical specimens are cut with respect to the longitudinal direction of the used bar. Their geometrical configurations and dimensions are directly given in Fig. 7. The cylindrical specimens are positioned vertically between the two platens of the testing machine. These tests are referred to as upsetting tests. During tests, the cylinders shorten in the axial direction and bulge in the lateral direction. The corresponding stress-strain curves are conducted at room temperature. Two different ratios of height to diameter (R= h/d)which are 1 and 1.5 are used.

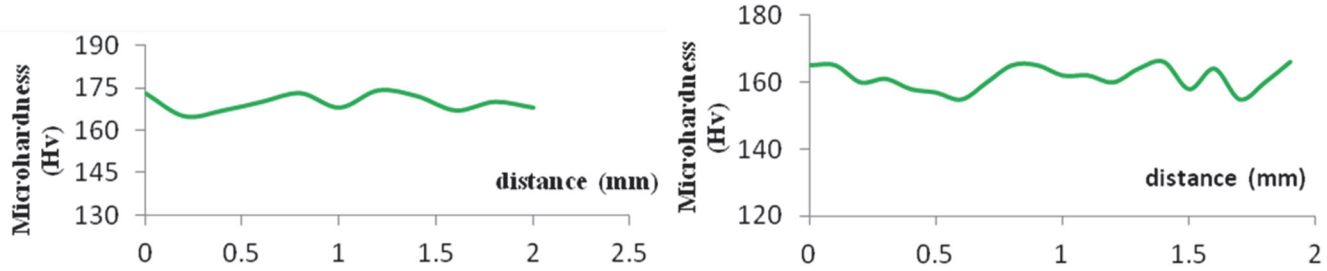

Figure 4: Micro hardness profile according to the two plans of 2017A-T4.

Directions	L	T
The average values (MVH)	126	128

Table 2: Average Micro hardness values in the longitudinal and transversal directions.

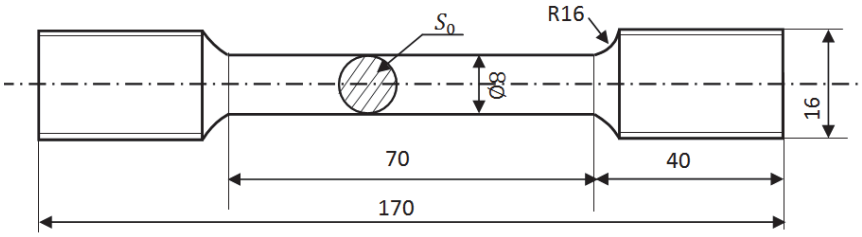

Figure 5: Geometry and dimensions of the specimen used for the tensile test.

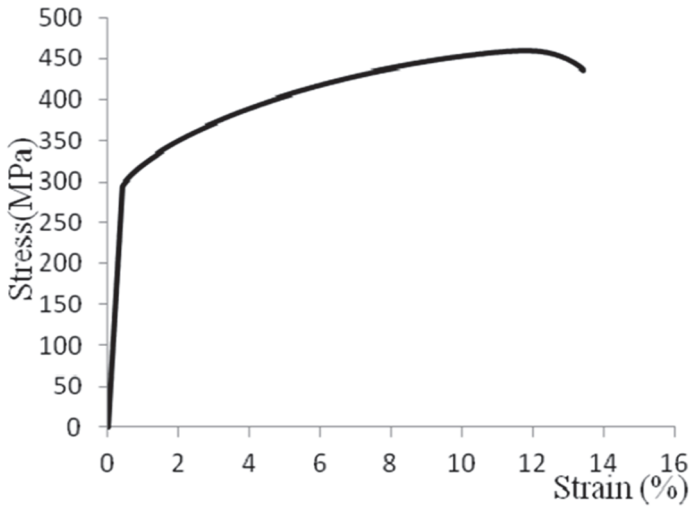

Figure 6: Stress-strain curve in tensile of the 2017A-T4 aluminum alloy.

Material	$\sigma_0\,(MPa)$	$\sigma_{ult}\,(MPa)$	$A_r\,(\%)$	$E(GPa)$	ν
2017A-T4	295	460	14	70	0.32

Table 3: Mechanical properties of the 2017A-T4.

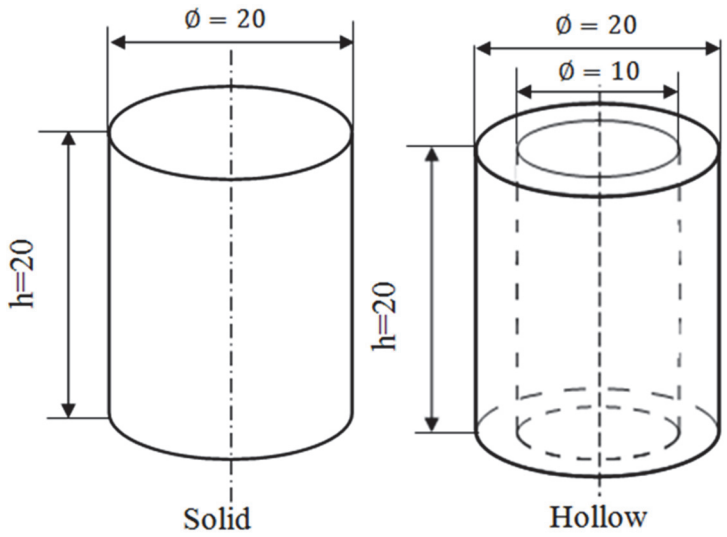

Figure 7: Type of specimens used according to the standard UNSL52905

Influence of the geometrical h/d ratio

The specimens with two ratios h/d are tested to study the effect of this geometrical parameter on the forming behavior of the 2017A-T4 aluminum alloy. Fig. 8 shows the evolution of the nominal stress versus the nominal strain for the hollow and solid cylinders. It is observed that the recorded stresses are higher with the decrease of h/d for the hollow cylinder. However, in the case of the solid specimens, the curves merge. This can be explained by the fact that in the hollow cylinder, for any plane perpendicular to the cylinder axis, the deformation mechanism occurs in two radial directions (outside and inside to fill the gap), while for the solid cylinder the flow mechanism takes place in the radial direction with respect to the outer surface only. Moreover, the obtained compressive strength for both cases is higher than the tensile strength.

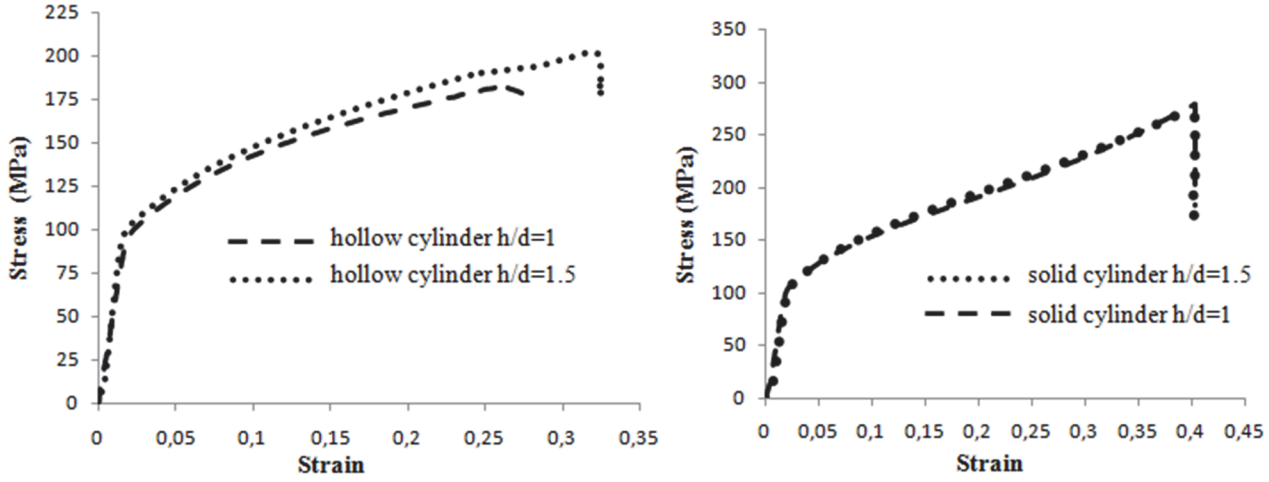

Figure 8: Nominal stress-strain curves for the solid and hollow cylinders, with two geometrical ratios of 1 and 1.5, under compression loadings.

Fracture under compression loading

From Fig.9, it is recognized that the deformed cylinders by the compressive load in the L direction lose the cylindrical shape and takes the well-known barrel shape. The aluminium alloy suffers from induced anisotropy due to plastic deformation. Then, the crack of a circular form known as annular crack appears on the surface of several tested cylinders. This has been also observed in [31].

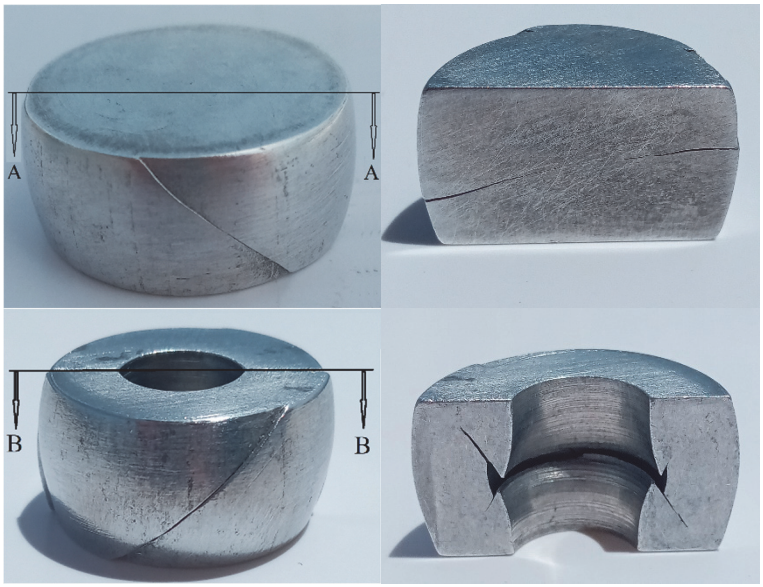

Figure 9: Cutaway views of upsetting specimens fractured show the direction and length of the crack.

The deformed specimens (solid and hollow) are cut showing the crack direction as well as its thickness starting from the surface as illustrated in Fig.9. In fact, two cross-sections of solid and hollow specimens give some details related to the formed cracks (Fig. 10) having almost a direction of 45° with respect to the loading axis.

Observation of fracture topographies from tensile and compression specimens

Observations through the SEM confirm the difference in fracture topographies of various specimens tested under tensile and compressive loads. These can be classified by the coexistence of two failure modes in compression (Fig. 11-a and Fig. 11-b) with different magnifications: oblique caused by the shear stress of the facets, where the sliding planes of the facets are compared to the others (areas1) and ductile with dimples (areas2), and by a ductile rupture with dimples under tension (Fig. 11-c). The fracture surface observation helps to understand the phenomena involved. The intergranular and intragranular fractures coexist in this configuration. Fracture surface analyses on the specimens performed by SEM reveal the presence of dimples confirming an intragranular ductile fracture. A careful examination of these dimples indicates the presence of a particle in a large number of cavities. Many large dimples are observed; the bottom shows coarse precipitates of θ-Al2Cu type.

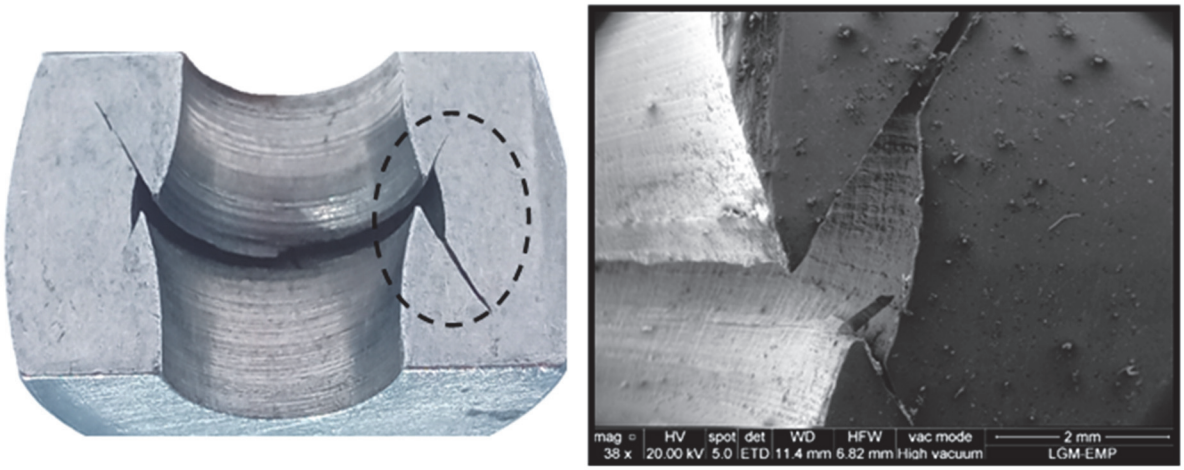

Figure 10: Details and type of crack observed in the hollow cylinders

The smooth areas also observed on the fracture surface show brittle fracture facets provoked by shear. These smooth areas become more under low triaxiality compared to high triaxiality. This is certainly due to the presence of precipitates. This provokes a brittle fracture, i.e., more intergranular ductile damage mode with coarse precipitates. Besides the intergranular damage mode, there is the presence of fine intragranular ligaments between the intergranular damage zones. According to the fracture surface observed by SEM (Fig.11), the induced anisotropy which may have contributed to the slant crack development is reported.

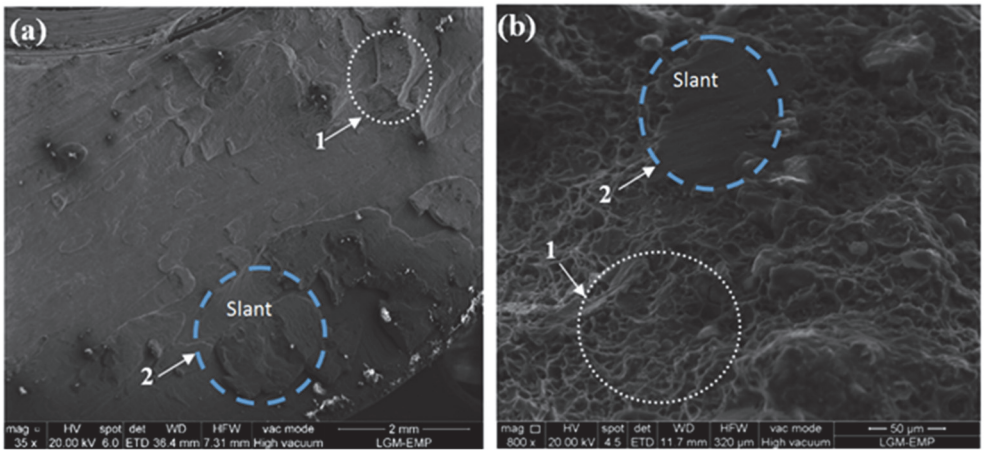

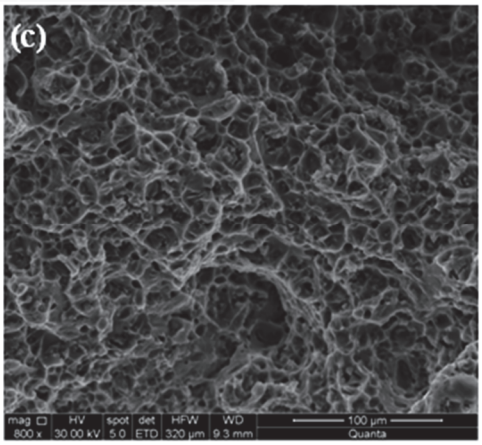

Figure 11: Fractography with the SEM of alloy 2017A-T4 tested. (a) and (b) in compression, (c) in tension.

In this part, macroscopic and microscopic characterizations assist also in identifying several parameters of the model. These parameters are used to describe the plastic damaged behavior controlled by the initial porosity and also by its evolution. On the other hand, the determination of the fracture mechanisms is naturally based on fracture topographies already given above.

NUMERICAL ASSESSMENT

Experimental observations show that the preponderant failure mode in the present study is related to shear mechanisms. In addition, due to the thermal heating of the billet during forming, known to promote the formation of shear bands [33], we use the extended GTN model incorporating shear mechanisms [35-37] which we have extended to take into account thermal heating. The predictions of this model are compared to those of the classical GTN model [9-11]. As adopted by Gurson in its original work [9], the assumption of rigid-plastic matrix behavior is adopted when formulating thermomechanical coupling. As a result, the thermo-mechanical behavior is modeled by formulating the plastic strain $\bar{\varepsilon}^p$ and temperature T expressions. The rate of change of plastic strain $\dot{\bar{\varepsilon}}^p$ is deduced using the microscopic and macroscopic plastic dissipation equivalence concept already proposed by Gurson [9]. The thermomechanical simulations are conducted in the framework of a sequential numerical scheme: the mechanical response is firstly calculated and the plastic dissipation estimated. Then, the variation of temperature induced by this dissipation is calculated.

The GTN model and its extension

Using the small-perturbation hypothesis concept, the functional form of the GTN modeling the case of a spheroidal Representative Volume Element (RVE) containing a confocal spheroidal cavity (Fig.12) is expressed by the following equations:

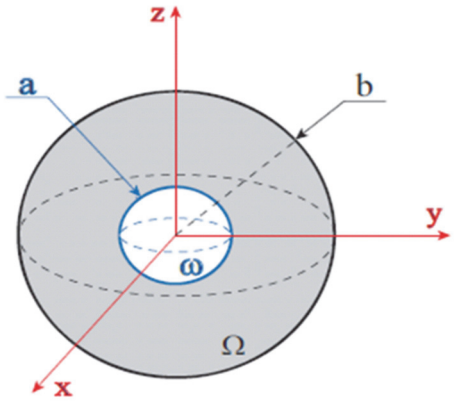

Figure 12: Geometry of the RVE considered in the GTN model (spherical voids)

$$\Phi(\Sigma_{eq},\Sigma_m,\bar{\sigma},f)=\left(\frac{\Sigma_{eq}}{\bar{\sigma}}\right)^2+2q_1f^*\cosh\left(\frac{3q_2\Sigma_m}{2\bar{\sigma}}\right)-1-\left(q_1f^*\right)^2=0 \quad (2)$$

where Σ_{eq} and Σ_m are the von Mises and mean stresses respectively, $\bar{\sigma}$ is the flow stress,q_1 and q_2 being coefficients introduced in [10-11] to take into account the interaction between neighboring cavities. f^* is a function proposed in [11] to describe the void coalescence:

$$f^*(f)=\begin{cases} f & if \quad f\le f_c \\ f_c+\delta(f-f_c) & if \quad f>f_c \end{cases} \quad (3)$$

where f is the porosity of the material, $\delta=\left(f_u-f_c\right)/\left(f_f-f_c\right)$.$f_u$ and f_c are the ultimate and critical volume fractions of voids. Taking into account the plastic incompressibility of the matrix, the porosity evolution law characterizing the damage growth can be written as [9]:

$$\dot{f}=(1-f)\dot{\varepsilon}^p_{kk} \quad (4)$$

where $\dot{\varepsilon}^p_{kk}$ represents the trace of the plastic strain rate tensor.

The plastic behavior law with hardening can be expressed via the concept of microscopic and macroscopic plastic dissipation equivalence [11].

$$\Sigma:\dot{E}^p=(1-f)\bar{\sigma}\,\dot{\bar{\varepsilon}}^p \quad (5)$$

where $\dot{\bar{\varepsilon}}^p$ the plastic strain rate of the material. Σ and $\dot{E}^p$ are the macroscopic stress and plastic strain rate tensors, respectively.

It's well known that damage accumulation along the loading path is a three-dimensional problem. Xue and Wierzbicki proposed an extension of the GTN model by considering the influence of three parameters (pressure, Lode angle, and equivalent stress) on the rate of change of damage [35-37]:

$$\dot{D}_{shear}=q_3f^{q_4}g_\theta\varepsilon_{eq}\dot{\varepsilon}_{eq} \quad (6)$$

The variable ε_{eq} represents the equivalent strain, g_θ is the Lode angle function introducing the dependence of the shear mechanism on the Lode angle, q_3 and $q_4$being material parameters [35]. If g_θ is not equal to zero, the shear mechanism is active and has to be considered in the calculation. However, if $g_\theta=0$, i.e., there is no shear mechanism effect, then the damage evolution is only related to the nucleation and growth of voids. The Lode angle function, g_θ, can be defined by [35-37]:

$$g_\theta=1-\frac{6|\theta|}{\pi}=1-\frac{2}{\pi}arccos\varpi \quad (7)$$

Moreover, the Lode angle expressed using the normalized third invariant of the deviatoric stress tensor (ϖ)is done by [35,36]:

$$\theta=\frac{1}{3}\arccos\xi \quad (8)$$

where ϖ is the ratio of the third invariant $J_3=\det(\Sigma')$ and the von Mises equivalent stress:

$$\varpi = \frac{27}{2}\frac{J_3}{\Sigma_{eq}^{\ 3}} \tag{9}$$

Σ' is the deviatoric stress tensor.
Due to the dependency of the loading history on the fracture initiation, the damage evolution is described in its rate form by:

$$\dot{D} = K_D\left(q_1 \dot{f} + \dot{D}_{shear}\right) \tag{10}$$

where K_D is the damage rate coefficient.
It is well known that the elastic properties of materials are affected by damage. However, this effect is negligible in a ductile rupture in comparison with the degradation caused by damage in the plastic zone. This assumption is also in concordance with the matrix rigid-plastic behavior adopted by Gurson in its original work.
In the coalescence phase, the damage evolves quickly to reach the critical damage value $D_c = q_1 f_c$ characterizing the rapid void volume growth. Thus, the damage rate coefficient can be deduced as [35-37]:

$$K_D = \begin{cases} 1 & \text{for} \quad D \le D_C \\ \dfrac{1/q_1 - f_c}{f_F - f_c} & \text{for} \quad D_C < D \le 1 \end{cases} \tag{11}$$

The present fracture models are based on the damage variable notion. The damage evolution rule is proposed in an integral form. Indeed, a linear relation linking the damage, *D*, and the equivalent plastic strain $\bar{\varepsilon}^{p}$ is expressed by

$$D = \int_0^{\bar{\varepsilon}^{p}} \frac{d\bar{\varepsilon}^{p}}{h(\eta,\theta)} \tag{12}$$

The total fracture is assumed to occur when $\bar{\varepsilon}^{p} = \bar{\varepsilon}_f$ ($\bar{\varepsilon}_f$ is the equivalent plastic strain at fracture) and *D=1* for any loading configuration, i.e., proportional or non-proportional loading path. In the case of proportional loading where the non-dimensional stress parameters η and $\bar{\theta}$ are constants, the explanation of the function $h(\eta,\bar{\theta})$ becomes straightforward. Indeed, for such a condition the integration of Eqn. (12) can be performed at the fracture point as: $\bar{\varepsilon}_f = h(\eta,\bar{\theta})$. The higher $\bar{\varepsilon}_f$, the lower the stress triaxiality. The function $\bar{\varepsilon}_f$ can be defined by five parameters, including four independent material parameters C_1, C_2, C_3 and C_4 as given by the following form [35,36]:

$$\bar{\varepsilon}_f(\eta,\varpi) = C_1 e^{-C_2\eta} - (C_1 e^{-C_2\eta} - C_3 e^{-C_4\eta})(1-\varpi^{1/\eta}) \tag{13}$$

Thermal heating due to plastic dissipation

In this paper, the GTN model and the GTN model modified by XUE are both extended considering the thermal evolution due to plastic dissipation. The model extension is formulated in the framework of the hypothesis adopted by Gurson considering a rigid-plastic matrix behavior, i.e. neglecting the elasticity effects. This hypothesis can also be found in its justification in this work by noticing that the dissipation of the inelastic work prevails over the thermo-elastic part in most bulk metal forming operations. So, the thermo-plastic coupling is conducted by adopting an overall isotropic matrix hardening characterized by the flow stress $\bar{\sigma}$ which depends on $\bar{\varepsilon}^{p}$ and the temperature (T) [30-32,38]: $\bar{\sigma} = \bar{\sigma}\left(\bar{\varepsilon}^{p}, T\right)$
With the absence of external heat sources, the temperature evolution law can be obtained by solving the general heat equation deducted from the first law of thermodynamics:

$$\rho C\dot{T} = -div(\mathcal{K}\mathrm{grad}T) + \xi\bar{\sigma}\,\dot{\bar{\varepsilon}}^{p} \tag{14}$$

$\mathcal{K}$ is the thermal conductivity, C the specific heat capacity and ρ the density of the material. ξ is the dimensionless inelastic heat fraction coefficient. ξ, also designed as the Taylor-Quinney coefficient, represents the fraction of plastic dissipation transformed to heat during material deformation. In finite element calculations, it's generally considered constant and varies from 0.85 to 0.95 for metals (see for instance [38-39]) and 0.3 to 0.7 for aluminum alloys [39]. However, some studies go on to consider ξ depending on the strain and/or strain rate [38-42].

Introduction of the thermoelasticity law

The thermoelastic law governing material behavior in the elastic domain is given by (see for instance) [30,43]:

$$\overset{\nabla}{\boldsymbol{\Sigma}} = \boldsymbol{\Lambda}^e : (\dot{\boldsymbol{E}} - \dot{\boldsymbol{E}}^{th}) + \frac{\partial \boldsymbol{\Lambda}^e}{\partial T} : (\boldsymbol{E} - \boldsymbol{E}^{th})\dot{T} \tag{15}$$

where $\boldsymbol{E}^{th} = \alpha(T - T_O)\mathbf{I}$ is the thermal strain tensor due to temperature expansion of the material and $\overset{\nabla}{\boldsymbol{\Sigma}}$ some objective time-derivative of the stress tensor $\boldsymbol{\Sigma}$. $\mathbf{I}$ is the second-order unit tensor. $\boldsymbol{\Lambda}^e$ is the elastic modulus tensor (stiffness tensor) of the material.

Assuming both thermal and mechanical isotropy and considering the dependence of the coefficient of linear thermal expansion α on temperature, the thermoelasticity law can be written by

$$\begin{aligned}\overset{\nabla}{\boldsymbol{\Sigma}} = {} & 2\left(G_0\dot{\boldsymbol{E}} + \frac{\partial G}{\partial T}\dot{T}\boldsymbol{E}\right) + \left[\left(K_0 - \frac{2}{3}G_0\right)tr\left(\dot{\boldsymbol{E}}\right) + \left(\frac{\partial K}{\partial T} - \frac{2}{3}\frac{\partial G}{\partial T}\right)\dot{T}tr\left(\boldsymbol{E}\right)\right]\mathbf{I} \\ & - \left(\gamma\alpha + 3K_0\frac{\partial \alpha}{\partial T}\Delta T + 3\frac{\partial K}{\partial T}\alpha\Delta T\right)\dot{T}\mathbf{I}\end{aligned} \tag{16}$$

G_0 is the classical initial (at ambient temperature) shear modulus and K_0 the initial bulk modulus. $\gamma = K_0\alpha$.

Numerical implementation

The GTN model and the GTN model modified by XUE both extended to incorporate material thermal heating due to mechanical dissipation are implemented into the ABAQUS/Explicit solver through a Vectorized User MATerial (VUMAT) Fortran-coded subroutine [44]. These are carried out using Aravas's algorithm [30, 43, 45] in the framework of a sequentially coupled thermal-stress algorithm. The mechanical equilibrium equation is firstly solved and the plastic dissipation is calculated by both spatial and time discretizations. Then, the temperature evolution is estimated at each element after resolving the heat equation as discussed in the Appendix A.

Particular attention is given to contact friction because of its role in metalworking processes. Indeed, several friction models have been developed for the quantitative evaluation of friction in metal forming. The Coulomb friction law (Eqn. 17) and constant friction model (Eqn. 18) are usually used in finite Element simulations [46].

$$\tau = \mu p \tag{17}$$

where τ is the frictional stress, μ is the coefficient of friction at the die/work-piece interface, and p is the normal stress.

The constant shear friction model (m-model) is done by:

$$\tau = mK \tag{18}$$

For $m = 1$, then $\tau = \tau_{\max} = K$ is the shear yield strength corresponding to the condition of maximum friction force, namely sticking friction. Whereas $m = 0$ means a frictionless condition. $K = \sigma_s/\sqrt{3}$ is the shear stress with σ_s being the yield strength.

From the above equations, the average Coulomb friction coefficient can be expressed using the friction factor (m) and the average surface pressure $\bar{P}$:

$$\mu = \frac{\sigma_s}{\overline{P}\sqrt{3}} m \tag{19}$$

This friction law has been commonly adopted for the simulation of forging processes. It has namely been shown that it gives appropriate results when describing these operations under high temperatures [47]. This law is adopted in this study.

Modeling the fracture of the specimens under compression

The GTN model and the GTN model modified by XUE both extended to incorporate thermomechanical effects due to plastic dissipation, referred to as GTN and GTN-Xue respectively, are used to study ductile fracture in bulk forming processes of the 2017A-T4 aluminum alloy. Solid and hollow cylindrical specimens with an initial height *h= 20mm* (see Fig. 13) are positioned between rigid tools. This assumption of rigidity seems to be reasonable due to the significantly higher mechanical properties of the tools compared to those of the aluminum alloy (experimentally, the material of upper and lower platens of the used machine has important stiffness and yield strength in comparison to the specimens). Due to the symmetry of the geometry and the loading, the calculation is carried out under axisymmetric conditions. The rigid tools are affected by a displacement *u* of 10mm under a quasi-static compressive velocity of 5mm/min. The specimens are meshed with axisymmetric solid elements with reduced integration CAXR.

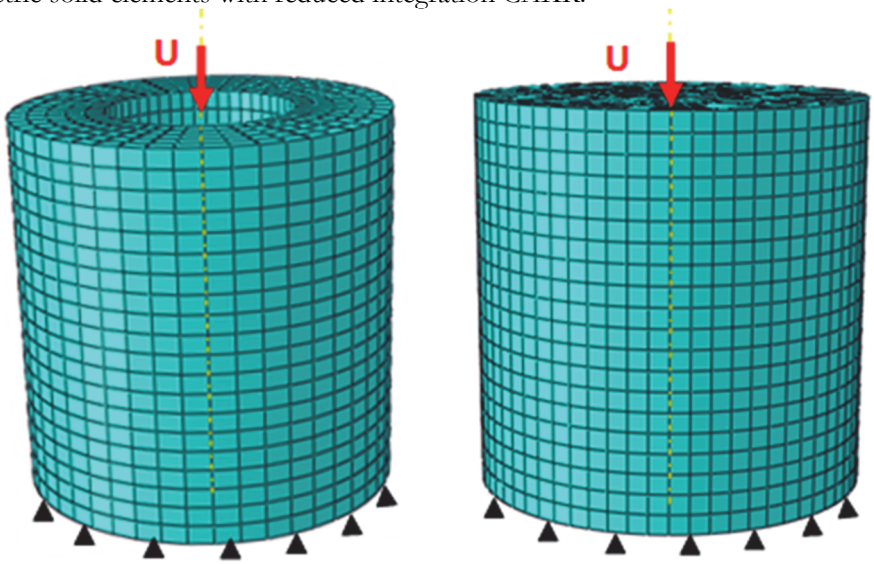

Figure 13: Shape of the work piece used in metal, initial mesh, initial mesh, the boundary conditions and loading

The damage and hardening material parameters are calibrated using the experimental tensile test results and then compared to numerical predictions of the two models presented above. Based on the conducted tensile tests, the material is characterized by the following coefficients: Young modulus E = 70 GPa, Poisson's ratio $\nu = 0.32$, yield stress σ_0 = 295 MPa, and hardening exponent $n = 0.134$. Due to the low temperature reached these properties are considered in this study temperature-independent. The initial material porosity f_0 is quantified with a measure of the voids rate in the plane perpendicular to the axis of the specimen. The main parameters obtained are recapitulated in Tab. 4.

Material parameters of the extended GTN and GTN-Xue models					
$f_0 = 0.015\%$	$f_c = 0.24\%$	$q_1 = 1.5$	$q_2 = 1$	$q_3 = 1.9$	$q_4 = 0.33$
$C_1 = 5.42$	$C_2 = 39.5$	$C_3 = 44$	$C_4 = 50$	$\xi = 0.5$	$\eta = 1/3$
$\varepsilon_N = 0.3$	$S_N = 0.1$	$C_v = 523\frac{J}{Kg.°K}$	$\alpha = 23.1\times10^{-6}\,°K$	$\lambda = 237\frac{W}{m}°K$	

Table 4: Material parameters of the GTN and GTN-Xue models coupled to the temperature

The flow stress law adopted is written:

$$\frac{\bar{\sigma}}{\sigma_o}=\left(1+\frac{\bar{\varepsilon}^{p}}{\varepsilon_o}\right)^{n}\left[1-\gamma\left(T-T_0\right)\right] \tag{20}$$

ε_o is the strain corresponding to σ_o and $T_o = 25°C$ the initial material temperature.

As mentioned above, the material parameters presented in Tab.3 are obtained by calibration of the numerical results with the experimental curve of tensile tests. The good concordance between the two curves shown in Fig.14 indicates the validity of the identification procedure.

In order to evaluate the ability of the GTN and GTN-Xue models to reproduce the material behavior during upsetting operations, numerical simulations are achieved on the cylindrical and hollow specimens with the two R ratios considered. Fig. (15, 16, 17, and 18) show comparisons between the numerical results and the experimental results representing the evolution of the applied force in the direction of the height reduction of the specimens.

For all the tests achieved in this study, the numerical predictions of the GTN and GTN-Xue models are compared to the experimental results obtained.

From all these comparisons, one can state that good agreement is found between experimental and numerical curves during the force evolution stage for the two models. However, the GTN model fails to capture the final workpieces' failure. In return, the GTN-Xue model can describe the final material rupture, when shear loading is present for all the tests.

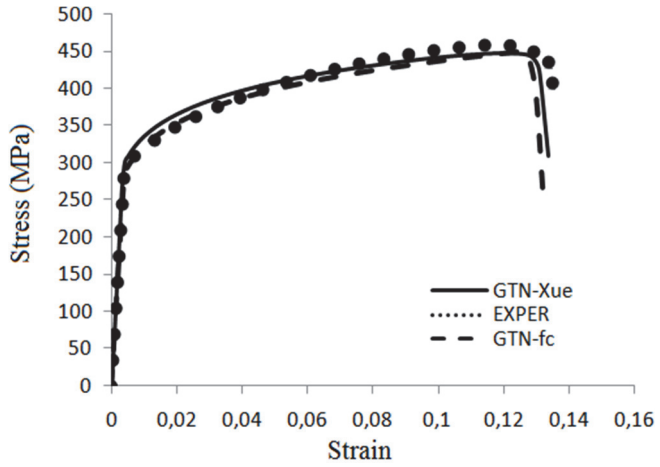

Figure 14: Determination of the material parameters of the GTN and extended GTN-Xue models by numerical calibration

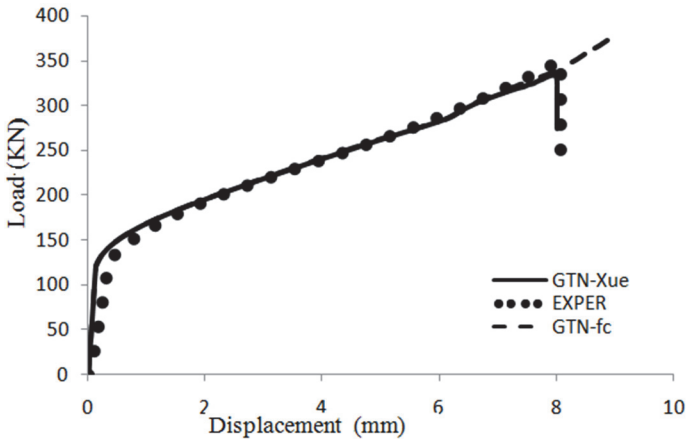

Figure 15: Force versus length-reduction for the solid specimens with the ratio h/d = 1.

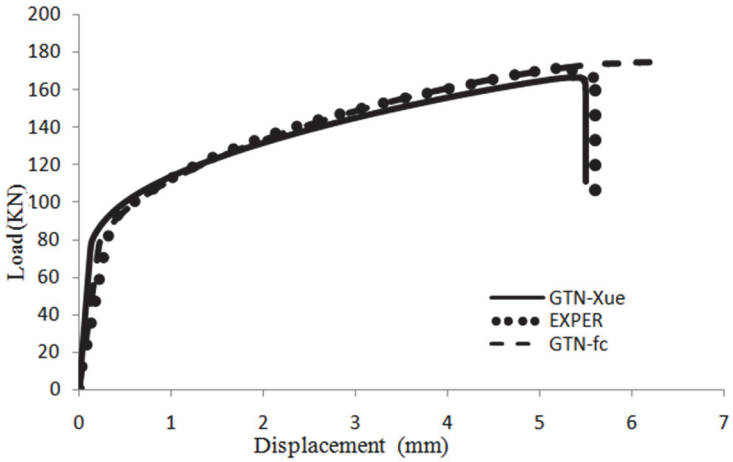

Figure 16: Force versus length-reduction for the hollow specimens with the ratio h/d = 1.

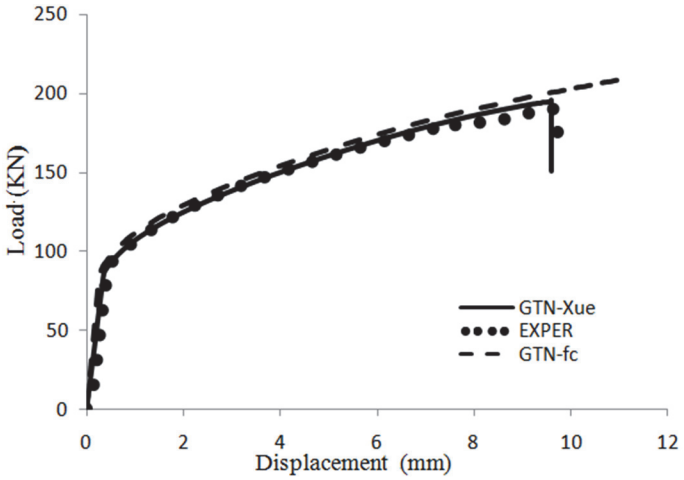

Figure 17: Force versus length-reduction for the solid specimens with the ratio h/d = 1.5.

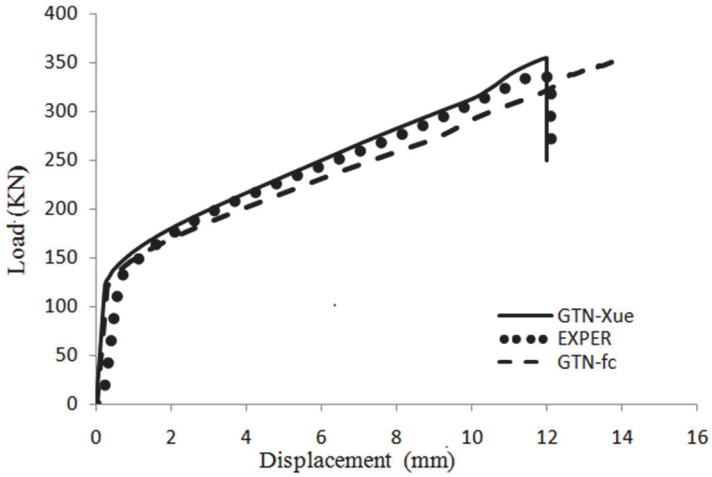

Figure 18: Force versus length-reduction for the hollow specimens with the ratio h/d = 1.5.

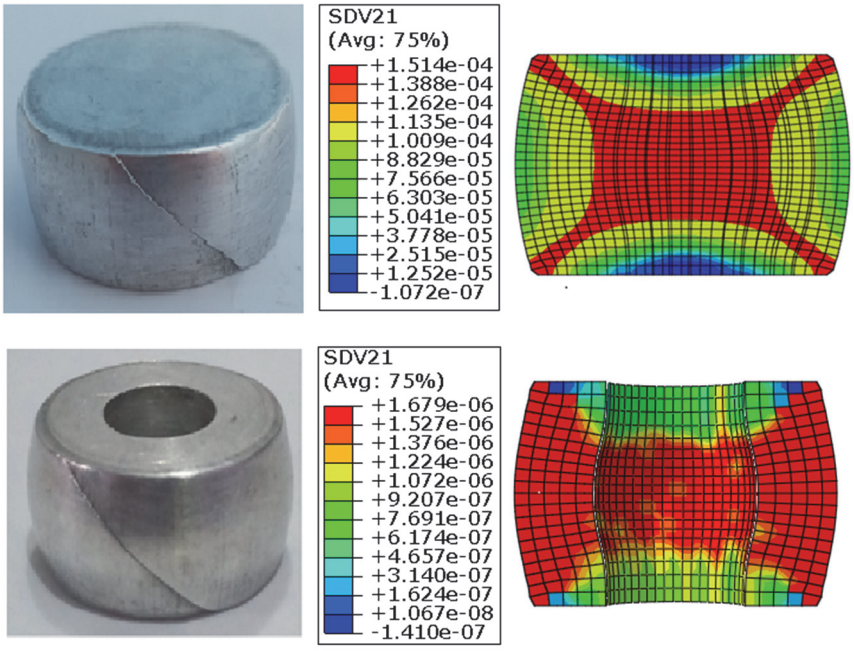

Figure 19: Distribution of the damage variable. Comparison with experimental results of cylindrical specimens.

Fig.19 represents the distribution of the damage variable calculated numerically with the GTN-Xue model and a photo at the fracture of a specimen subjected experimentally to the forging process. The damage zone is also correctly predicted by this model which comforts the previous results of slant fracture of both the solid and hollow specimens.

Conclusion

In this paper, the ductile fracture of the 2017A-T4 aluminum alloy subjected to forging operations experimentally and numerically studied. An experimental methodology consisting of several tensile and compression tests has been carried out and analyzed. Compression tests are employed to study the forging process. The numerical simulations are conducted using two physically-based damage models, both extended to include thermal heating due to mechanical dissipation. The first one is the physically-based Gurson-Tvergaard-Needleman (GTN) model describing the nucleation, growth, and coalescence of cavities during material deformation. The second is an improvement of the GTN model, modified to incorporate the shear mechanism. Both theoretical and numerical aspects are presented. The experimental procedure used in the identification of the models parameters is clearly explained.

The shear mechanism is assumed to be controlled by the equivalent plastic strain, stress triaxiality, and Lode angle [35-37]. However, in cold forged parts, the heat gradient(heat dissipation) raises during this manufacturing process. It is then essential to include the influence of temperature in the metal behaviourmodel. In the same way, the formation of shear bands in metals is favored by the thermal heating of the material. So as a consequence, in the second constitutive law, the evolution of damage by shear is implicitly coupled to the temperature which induces thermally softening in shear.

The main conclusions can be stated as:

1) The well-known barrel shape is gotten when a compressive load is applied in the axial direction of cylindrical specimens.
2) In the case of cylindrical pieces under compression, the circular-shaped crack known as annular crack appears on the surface. This is related to the anisotropy induced by plastic deformation.
3) The formed cracks have almost a direction of 45° with respect to the loading direction in the two cases of solid and hollow specimens
4) SEM analyses of fracture topographies show a ductile fracture with dimples under tension and coexistence of two fracture modes under compression: ductile with dimples (Fig. 11) and slant induced by the shear stress of the facets.
5) The presence of dimples confirms an intragranular ductile fracture. However, the smooth areas also observed on the fracture surface showed brittle fracture facets induced by shear. This is due to the presence of precipitates that

induce a brittle fracture. So, besides the intergranular damage mode, there is the presence of fine intragranular ligaments between the intergranular damage zones.

6) An anisotropy that may have contributed to the slant crack development is also observed.
7) The comparison of the numerical predictions with the experimental results of forging of solid and hollow blanks shows the capacity of the two micromechanical models to correctly describe the forming force of the blanks (growth stage of the force). However, the GTN model fails to capture the final failure of the material, unlike the GTN-Xue model which incorporates shear mechanisms.

ACKNOWLEDGMENT

The authors would like to acknowledge the helpful discussion with Prof. A. Abdul-Latif from Laboratory Quartz, Supmeca - Paris 8 University, FRANCE.

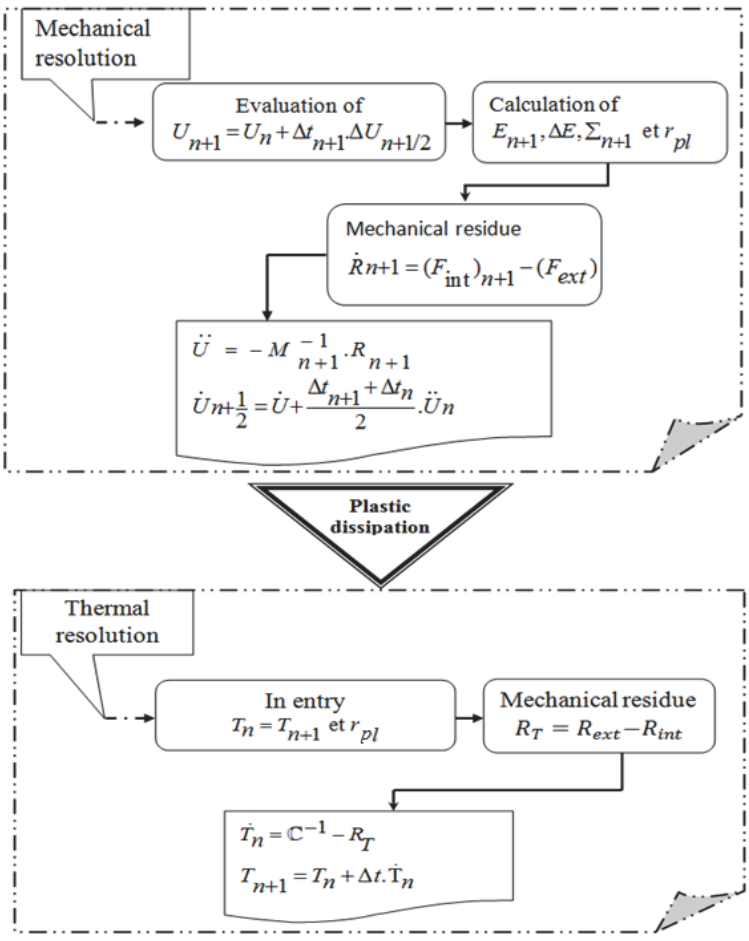

Figure A-1:Flow chart of the model implementation

APPENDIX A

A.1) Mechanical problem

The spatial discretization of the mechanical equilibrium equation leads to the matrix system:

$$\boldsymbol{M}\ddot{\boldsymbol{U}}+\boldsymbol{F}_{\text{int}}-\boldsymbol{F}_{ext}=0 \tag{A.1}$$

where $\boldsymbol{M}$ and $\boldsymbol{F}_{ext}$ being respectively the classical consistent matrix mass, internal and external forces vectors.
The temporal resolution of Eqn. (A.1) with an explicit dynamic numerical scheme can be obtained by solving the equations below:

$$\ddot{\boldsymbol{U}}_n = \boldsymbol{M}_n^{-1}\left(\boldsymbol{F}_{\text{int}} - \boldsymbol{F}_{ext}\right) \tag{A.2}$$

$$\dot{\boldsymbol{U}}_{n+\frac{1}{2}} = \dot{\boldsymbol{U}}_{n-\frac{1}{2}} + \frac{\Delta t_{n+1} + \Delta t_n}{2}\ddot{\boldsymbol{U}}_n \tag{A.3}$$

$$\boldsymbol{U}_{n+1} = \boldsymbol{U}_n + \Delta t_{n+1}\dot{\boldsymbol{U}}_{n+\frac{1}{2}} \tag{A.4}$$

The solution of Eqns. (A.2- A.4) t_n requires the evaluation of the stress tensor $\boldsymbol{F}_{\text{int}}$ at each time t_n, using the implemented micromechanical models.

A.2) Thermal problem

Consider a solid volume V submits to a heat flux q_f .The sequential resolution diagram of a thermomechanical problem is employed. The principle of such an algorithm is to calculate the mechanical behavior, and then the thermal effect is deduced after evaluation of the mechanical dissipation. The resolution of the thermal problem is based on the resolution of the heat equation given by Eqn. 14.
Real and virtual temperatures at any point of the solid V are connected to the movement of adjacent nodes by appropriate functions. Therefore, the Galerkin method is used: $\boldsymbol{T}^e = \boldsymbol{N}_n^{q_f}\boldsymbol{T}_n^e$ and $\delta\boldsymbol{T}^e = \boldsymbol{N}_n^{q_f}\delta\boldsymbol{T}_n^e$, where $\boldsymbol{N}_n^{q_f}$ are the temperature nodal interpolation functions for the element (e). These functions depend on the spatial coordinates expressed in the reference space. $\boldsymbol{T}_n^e$ designates the temperature vector for each node.
The overall equilibrium of the total structure is obtained by adding all quantities of all the elements.

$$\boldsymbol{J} = \sum_e \boldsymbol{J}_e = \left[\sum_e (\boldsymbol{C}^e \dot{T}^e + \boldsymbol{R}_{\text{int}}^e - \boldsymbol{R}_{ext}^e)\right]\delta\boldsymbol{T}^e = 0 \tag{A.5}$$

where

$$\boldsymbol{C}^e = \int_{V_e} \rho C_v {}^T\boldsymbol{N}_n^{q_f}\boldsymbol{N}_n^{q_f}\, dV \tag{A.6}$$

$$\boldsymbol{R}_{ext}^e = \int_{V_e} {}^T\boldsymbol{N}_n^{q_f}\,\Psi \mathrm{dV} \tag{A.7}$$

$$\boldsymbol{R}_{\text{int}}^e = \int_{\Gamma_T} {}^T\boldsymbol{N}_n^{q_f}\,\overline{q}_f dT + \int_{V_e} {}^T\boldsymbol{Z}_n^e\left(\mathcal{K}T\right)\boldsymbol{Z}_n^e dV - \int_{V_e} {}^T\boldsymbol{N}_n^{q_f}\, r_{pl} dV + \int_{\Gamma_q} {}^T\boldsymbol{N}_n^{q_f}\, q_f dT \tag{A.9}$$

where $\boldsymbol{C}^e$ is the matrix elementary capacitance. In Eqn. (A.9), r_{pl} represent the plastic dissipation.

A.3) Thermomechanical problem

For the adopted strategy of the resolution, the explicit resolution flowchart of the model equation is summarized in Fig.A.1. It illustrates the sequential coupling between the mechanical and the thermal resolutions.

APPENDIX B: IMPLEMENTATION OF THE CONSTITUTIVE MODEL

The following convention is considered by replacing the volume fraction $q_1 f^*$ with the damage variable D. In fact, the total fracture occurs when D= 1. Therefore, the critical void volume fraction of voids f_c will correspond $D_c = q_1 f_c$. Hence, Eqn. (2) can be rewritten as:

$$\Phi\left(\Sigma^e_{eq},\Sigma^e_m,\bar{\sigma},D\right)=\left(\frac{\Sigma^e_{eq}}{\bar{\sigma}}\right)^2+2D\cosh\left(\frac{3q_2\Sigma^e_m}{2\bar{\sigma}}\right)-\left(1+D^2\right)=0 \tag{B.1}$$

The implementation procedure details of the stress update algorithm are demonstrated below [30, 43, 45].

1. Get initial values at t=0,…,t_i

$$\boldsymbol{\Sigma}^e_t,\boldsymbol{E}_t,\Delta\boldsymbol{E}_{t+\Delta t},\bar{\sigma}_t,f_t,D_t$$

2. The trial elastic stress tensor Σ^e under the assumption of thermoelastic strain increment is evaluated as follows:

$$\boldsymbol{\Sigma}^e{}_{t+\Delta t}=\boldsymbol{\Sigma}^e{}_t+\frac{\partial\boldsymbol{\Lambda}^e}{\partial T}:(\dot{\boldsymbol{E}}_{t+\Delta t}-\dot{\boldsymbol{E}}^{th}_{t+\Delta t})\Delta T_{t+\Delta t}+\boldsymbol{\Lambda}^e:\left(\Delta\boldsymbol{E}_{t+\Delta t}-\Delta\boldsymbol{E}^{th}_{t+\Delta t}\right) \tag{B.2}$$

3. Calculation of the hydrostatic stress $\Sigma^e_{m,t+\Delta t}$ and equivalent stress $\Sigma^e_{eq},_{t+\Delta t}$ of total trial stress Σ^e_{eq} to evaluate the yield potential:

$$\Sigma^e_{m,t+\Delta t}=-\frac{1}{3}\boldsymbol{\Sigma}^e_{t+\Delta t}:\mathbf{I}$$

$$\Sigma^e_{eq},_{t+\Delta t}=\sqrt{\frac{3}{2}\boldsymbol{\Sigma}^{'}_{t+\Delta t}:\boldsymbol{\Sigma}^{'}_{t+\Delta t}}$$

where $\boldsymbol{\Sigma}^{'}=\boldsymbol{\Sigma}^e-\frac{1}{3}\mathrm{tr}(\boldsymbol{\Sigma}^e)$ is the deviatoric part of the trial stress tensor $\boldsymbol{\Sigma}^e$.

4. Calculation of the yield potential (Eqn.B.1) and checking the current (updated) state:

If $\Phi_{t+\Delta t}\le 0$, this leads to the fact that the current time step is elastic, while for $\Phi_{t+\Delta t}>0$, the material is plasticized, and then go to step 5 to continue the plastic calculation.

5. Plastic correction

For sake of simplification, the subscript $t+\Delta t$ is omitted in what follows.

a. flow direction:

$$\boldsymbol{N}=3\boldsymbol{\Sigma}'/2\Sigma_{eq} \tag{B.3}$$

b. The nonlinear Eqns. (B.4) and (B.5) are resolved simultaneously using the Newton-Raphson iterative method.

$$\Delta E^{i+1}_p\frac{\partial\Phi}{\partial\Sigma_{eq}}+\Delta E^{i+1}_q\frac{\partial\Phi}{\partial\Sigma_m}=0 \tag{B.4}$$

$$\Phi\left(\Sigma^{i+1}_m,\Sigma^{i+1}_{eq},\bar{\sigma},f,D\right)=0 \tag{B.5}$$

5. Update the hydrostatic stress Σ_m, the equivalent stress Σ_{eq}:

$$\begin{cases} \Sigma_m = \Sigma_m^e + K\Delta E_p \\ \Sigma_{eq} = \Sigma_{eq}^e - 3G\Delta E_q \end{cases} \tag{B.6}$$

and the variables $\bar{\sigma}, f, D$ statement:

$$\begin{cases} \Delta\bar{\sigma} = \left(\dfrac{\hbar_\varepsilon}{\bar{\sigma}} + \hbar_T \dfrac{\xi}{\rho c_v} \right) \dfrac{-\Sigma_m \Delta E_p + \Sigma_{eq} \Delta E_q}{(1-f)} \\ \Delta f = (1-f)\Delta E_p + \mathcal{A}\Delta E_m^{pl} \\ \Delta D = K_D \left[\Delta f + q_3 f^{q_4} g(\theta) \varepsilon_{eq} \dot{\varepsilon}_{eq} \right] \end{cases} \tag{B.7}$$

where $\hbar_\varepsilon = \dfrac{\partial\bar{\sigma}}{\partial\bar{\varepsilon}^p}$ is the plastic modulus at constant temperature and $\hbar_T = \dfrac{\partial\bar{\sigma}}{\partial T}$ the temperature modulus at constant strain.

REFERENCES

[1] Yang, S., Yi, D., Zhang, H., Yao, S. (2008). Flow stress behavior and processing map of Al-Cu-Mg-Ag alloy during hot compression. Journal of Wuhan University of Technology, Mater. Sci., 23(5), pp.694–698. DOI: 10.1007/s11595-007-5694-x.

[2] Boschetto, A., Bottini, L., Campana, F., Consorti, L., Pilone, D. (2013). Investigation via morphological analysis of aluminium foams produced by replication casting, Frattura ed Integrità Strutturale, 26, pp.1-11. DOI: 10.3221/IGF-ESIS.26.01.

[3] Belouettar, K., Ould Ouali, M., Zeroudi, N., Thibaud, S. (2021), Investigation of the influence of incremental sheet forming process parameters using response surface methodology, Metallurgical Research and Technolog., 118(4),pp.401. DOI: 10.1051/metal/2021039.

[4] Salmi, A., Elajrami, M., Slimani, M.E.A. (2019). Crack growth study under thermo-mechanical loads: parametric analysis for 2024 T3 aluminum alloy, Frattura ed Integrità Strutturale, 50, pp.231-241. DOI: 10.3221/IGF-ESIS.50.19.

[5] Peñuelas, I., Betegón, C., Rodríguez, C. (2006). A ductile failure model applied to the determination of the fracture toughness of welded joints, Numerical simulation and experimental validation. Engineering Fracture Mechanics, 73(18), pp.2756-2773. DOI: 10.1016/j.engfracmech.2006.05.007.

[6] Bordonaro, G. G., Leardi, R., Diviani, L., Berto, F. (2018). Design of Experiment as a powerful tool when applying Finite Element Method: a case study on prediction of hot rolling process parameters, Frattura ed Integrità Strutturale, 12(44), pp.1–15. DOI: 10.3221/IGF-ESIS.44.01.

[7] Abdul-Latif, A., Ahmed-Ali, A., Baleh, R., Ould Ouali, M. (2017). Innovative solution for strength enhancement of metallic like-composite tubular structures axially crushed used as energy dissipating devices, Journal Thin-Walled Structures, 119, pp. 332–344. DOI: 10.1016/j.tws.2017.06.024

[8] Zerouki, M., Ould Ouali, M., Benabou, L. (2020). Metallurgical Phase Transformation and Behavior of Steels Under Impact Loading, Metallurgical and Materials Transactions A: Physical Metallurgy and Materials Science, 51(1), pp. 252-262. DOI: 10.1007/s11661-019-05527-z.

[9] Gurson, A.L., (1977). Continuum theory of ductile rupture by void nucleation and growth: Part I- yield criteria and flow rules for porous ductile media, ASME J. Engineering Materials Technology., 99, pp. 2-15. DOI: 10.1115/1.3443401.

[10] Tvergaard, V. (1981). Influence of voids on shear bands instabilities under plane strain conditions, Int. J. Fracture., 17, pp.389–407. DOI: 10.1007/BF00036191.

[11] Tvergaard, V., Needleman, A. (1984). Analysis of the cup-cone fracture in a round tensile bar, Acta Metallurgica., 32, pp.157–169. DOI: 10.1016/0001-6160(84)90213-X.
[12] Torki, M. E., Benzerga, A. A., Leblond, J.-B. (2015). On Void Coalescence under Combined Tension and Shear, J. Appl. Mech., 82(7), pp.15. DOI: 10.1115/1.4030326.
[13] Torki, M., Keralavarma, S., Benzerga, A. (2021). An analysis of Lode effects in ductile failure, Journal of the Mechanics and Physics of Solids, 153(11), 104468. DOI: 10.1016/j.jmps.2021.104468.
[14] Torki, M., Benzerga, A. A. (2022). Ductile Fracture in Plane Stress, J. Appl. Mech., 89(1): 011001, pp. 11. DOI: 10.1115/1.4052106.
[15] Keralavarma, S., Reddi, D., Benzerga, A.A. (2020). Ductile failure as a constitutive instability in porous plastic solids, Journal of the Mechanics and Physics of Solids, 139(6), 103917. DOI: 10.1016/j.jmps.2020.103917.
[16] Monchiet, V., Charkaluk, E., Kondo D. (2011). A micromechanics-based modification of the Gurson criterion by using Eshelby-like velocity fields, European J. of Mechanics A/Solids., 30, pp. 940-949. DOI: 10.1016/j.euromechsol.2011.05.008
[17] Benzerga, A. A., Leblond, J.B. (2010). Ductile Fracture by Void Growth to Coalescence, In: Advances in Applied Mechanics, 44, pp.169–305. DOI: 10.1016/S0065-2156(10)44003-X
[18] Torki, M. E., Benzerga, A. A., Leblond, J.-B. (2015). On Void Coalescence under Combined Tension and Shear, J. Appl. Mech. 82(7). DOI: 10.1115/1.4030326
[19] Cricrì, G.. (2013). A consistent use of the Gurson-Tvergaard-Needleman damage model for the R-curve calculation, Frattura ed Integrità Strutturale, 24, pp.161-174. DOI: 10.3221/IGF-ESIS.24.17.
[20] Gologanu, M., Leblond, J.-B., Perrin, G., Devaux, J. (1997). Recent extensions of Gurson's model for porous ductile metals, In: Suquet, P. (Ed.), Continuum Micromechanics, Springer., pp.61–130. DOI: 10.1007/978-3-7091-2662-2_2.
[21] Pardoen, T., Hutchinson, J.W. (2000). An extended model for void growth and coalescence, J. Mech. and Phy. Solids., 48, pp.2467–2512. DOI: 10.1016/S0022-5096(00)00019-3.
[22] Nahshon, K., Hutchinson, J.W. (2008). Modification of the Gurson model for shear failure, Eur J Mech A-Solid., 27, pp.1–17. DOI: 10.1016/j.euromechsol.2007.08.002.
[23] Wierzbicki, T., Xue, L. (2005), On the effect of the third invariant of the stress deviator on ductile fracture. Technical Report, Impact and Crashworthiness Lab, MIT., 136.
[24] Wilkins, M.L., Streit, R.D., Reaugh, J.E. (1980). Cumulative-strain-damage model of ductile fracture: simulation and prediction of engineering fracture tests. Technical Report UCRL-53058, Lawrence Livermore National Laboratory, pp.69. DOI: 10.2172/6628920.
[25] Bai, YL., Dodd, B. (1992). Adiabatic shear localization. Theories and Applications, Oxford: Pergamon Press.
[26] Meyers, MA. (1994). Dynamic behavior of materials. New York, Wiley.
[27] Wright, TW. (2002). The physics and mathematics of adiabatic shear bands. Cambridge: Cambridge University Press.
[28] Bethmont, M., Rousselier, G., Devesa, G., Batisse, R. (1987). Ductile fracture analysis by means of a local approach. In: 9th int. conf. on structural mechanics in reactor technology, SMIRT9, Lausannne, 105(1), pp 113-120, pp.131–141. DOI: 10.1016/0029-5493(87)90235-4.
[29] Huber, G., Brechet, Y., Pardoen, T. (2005) Predictive model for void nucleation and void growth controlled ductility in quasi-eutectic cast aluminium alloys, Acta Mater., 53, pp. 2739–2749. DOI: 10.1016/j.actamat.2005.02.037.
[30] Ould Ouali, M., Aberkane, M. (2009). Micromechanical modeling of the rolling of a A1050P aluminum sheet, International Journal of Material Forming, 2(1), pp.25-36. DOI: 10.1007/s12289-008-0387-3.
[31] Pérez-Castellanos, J.-L. (2012). Temperature increase associated with plastic deformation under dynamic compression: application to aluminium alloy Al 6082, Journal of Theoretical and Applied Mechanics, 50(2), pp.377-398.
[32] Rusinek, A. Klepaczko, J.R. (2009). Experiments on heat generated during plastic deformation and stored energy for TRIP steels, Materials and Design., 30, pp. 35-48. DOI: 10.1016/j.matdes. 2008.04.048.
[33] Batra, RC., Wei, ZG. (2006). Shear band spacing in thermoviscoplastic materials, Int J Impact Eng., 32, pp. 947–967. DOI: 10.1016/j.ijimpeng.2004.08.001.
[34] Benzerga, A.A., Besson, J., Pineau, A. (2004). Anisotropic ductile fracture: Part I: experiments, Acta Materialia, 52 (15), pp.4623-4638. DOI: 10.1016/j.actamat.2004.06.020.
[35] Xue, L. (2008). Constitutive modeling of void shearing effect in ductile fracture of porous materials, Engineering Fracture Mechanics, 75, pp. 3343–3366. DOI: 10.1016/j.engfracmech.2007.07.022.
[36] Xue, L., Wierzbicki, T. (2009). Ductile fracture characterization of aluminum alloy 2024-T351 using damage plasticity theory, Int. J.of Applied Mechanics,1, pp. 267-304. DOI: 10.1142/S1758825109000198.

[37] Bai, Y., Wierzbicki, T. (2007). A new model of metal plasticity and fracture with pressure and Lode dependence, Int. J. Plasticity, 24, pp. 1071-1096. DOI: 10.1016/j.ijplas.2007.09.004
[38] Zaera, R., Rodríguez-Martínez, J.A., Rittel. D. (2013). On the Taylor–Quinney coefficient in dynamically phase transforming materials. Application to 304 stainless steel, Inter. J. of Plasticity, 40, pp.185-201. DOI: 10.1016/j.ijplas.2012.08.003.
[39] Hodowany, J., Ravichandran, G., Rosakis, A.J., Rosakis, P. (2000). Partition of plastic work into heat and stored energy in metals, Exp. Mech. 40, pp.113–123. DOI: 10.1007/BF02325036
[40] Sornin, D., Karch, A., Nunes, D. (2015). Finite element method simulation of the hot extrusion of a powder metallurgy stainless steel grade, International Journal of Material Forming, 8(1), pp.145–155. DOI: 10.1007/s12289-013-1156-5
[41] Vivier, G., Trumel, H., Hild, F. (2009). On the stored and dissipated energies in heterogeneous rate-independent systems. Theory and simple examples, Continuum Mechanics and Thermodynamics, 20 (7), pp.411-427. DOI: 10.1007/s00161-008-0089-6
[42] Rosakis, P., Rosakis, A.J., Ravichandran, G., Hodowany, J. (2000). A thermodynamic internal variable model for the partition of plastic work into heat and stored energy in metals, Journal of the Mechanics and Physics of Solids, 48(3), pp.581-607. DOI: 10.1016/S0022-5096(99)00048-4.
[43] Ould Ouali, M. (2018). Relevance of incorporating cavity shape change in modelling the ductile failure of metals, Mathematical Problems in Engineering, pp. 1-9. DOI: 10.1155/2018/6454790.
[44] Abaqus 2019 User's manuals. Dassault Systèmes Simulia Corp. Providence, RI, USA. http://www.simulia.com/locations/locations.html.
[45] Aravas, N. (1987). On the numerical integration of a class of pressure dependent plasticity models, Int. J. Numerical Methods in Engineering., 24, pp 1395-1416. DOI: 10.1002/nme.1620240713
[46] Tan, X. (2002). Comparisons of friction models in bulk metal forming. Tribol. Int., 35, pp 385–393. DOI: 10.1016/S0301-679X(02)00020-8.
[47] Sethy, R., Galdos, L., Mendiguren, J. de Argandoña, E. S. (2016). Investigation of influencing factors on friction during ring test in hot forging using FEM simulation, AIP Conference Proceedings 1769, 130009. DOI: 10.1063/1.4963528.